

Radio Imaging of the NGC 1333 IRAS 4A Region: Envelope, Disks, and Outflows of a Protostellar Binary System

Minho CHOI^{1,2}, Miju KANG¹, Ken'ichi TATEMATSU³, Jeong-Eun LEE⁴, and Geumsook PARK⁵

¹*Korea Astronomy and Space Science Institute, 776 Daedeokdaero, Yuseong, Daejeon 305-348, South Korea*
minho@kasi.re.kr

²*University of Science and Technology, 217 Gajeongro, Yuseong, Daejeon 305-350, South Korea*

³*National Astronomical Observatory of Japan, 2-21-1 Osawa, Mitaka, Tokyo 181-8588, Japan*

⁴*Department of Astronomy and Space Science, Kyung Hee University, Yongin, Gyeonggi 446-701, South Korea*

⁵*Department of Physics and Astronomy, Seoul National University, Seoul 151-742, South Korea*

Abstract

The NGC 1333 IRAS 4A protobinary was observed in the 1.3 cm and 6.9 mm continuum and the ammonia and SiO lines, with an angular resolution of about 0.4 arcseconds. The continuum maps show the circumstellar structures of the two protostars, A1 and A2. The A1 system is brighter and more massive than the A2 system. The ratio of mass, including dense gas and protostar, is about 6. The properties of the circumstellar disks and outflows suggest that A1 may be younger than A2. The deflected part of the northeastern jet of A2 is bright in the SiO line, and the distance between the brightest peak and deflection point suggests that the enhancement of SiO takes about 100 yr after the collision with a dense core. The ammonia maps show a small structure that seems to be a part of the obstructing core. The outflow properties were studied by comparing interferometric maps of SiO, ammonia, formaldehyde, and HCN lines. Their overall structures agree well, suggesting that these species are excited by the same mechanism. However, the intensity distributions show that SiO is chemically unique. SiO may be directly linked to the primary jet while the other species may be tracing the entrained ambient gas.

Key words: ISM: individual (NGC 1333 IRAS 4A) — ISM: jets and outflows — ISM: structure — stars: binaries: general — stars: formation

1. INTRODUCTION

NGC 1333 IRAS 4A2 is one of the best-studied low-mass protostars. It has a circumstellar disk viewed nearly edge-on and drives a well-collimated and rotating outflow/jet (Choi 2005; Choi et al. 2007, 2011). Choi et al. (2010) found that the NH₃ (2, 2) and (3, 3) lines seem to selectively trace the accretion disk while the millimeter/centimeter continuum seems to trace both disk and envelope. The rotation kinematics of the disk suggests that the mass of the central protostar is $\sim 0.08 M_{\odot}$ and that the collapse age is $\sim 50,000$ yr (Choi et al. 2010). The bipolar jet flows in the northeast-southwest direction (Blake et al. 1995; Hodapp & Ladd 1995; Lefloch et al. 1998). The jet may be launched from a small region on the disk, or outflow foot-ring, with a radius of ~ 2 AU (Choi et al. 2011). The northeastern jet shows a sharp bend of flow direction that may be caused by a collision with a dense core in the ambient cloud (Choi 2005; Baek et al. 2009). IRAS 4A2 also exhibits other star formation activities such as H₂O maser emission (Park & Choi 2007; Marvel et al. 2008).

IRAS 4A2 belongs to a binary system (IRAS 4A) in the Perseus star-forming region at a distance of 235 pc from the Sun (Lay et al. 1995; Looney et al. 2000; Hirota et al. 2008). The spectral energy distribution of IRAS 4A suggests that the constituent binary members are Class 0 protostars (Sandell et al. 1991; Enoch et al. 2009). The luminosity of IRAS 4A suggests that the protostars are growing at a rate typical of Sun-like stars through the accretion of gas from the molecular envelope (Jennings et al. 1987; Choi et al. 2010).

IRAS 4A1 is brighter in the millimeter/centimeter continuum than its sibling protostar A2 (Looney et al. 2000; Reipurth et al. 2002; Jørgensen et al. 2007), but it is weaker in the NH₃ emission (Choi et al. 2007). IRAS 4A1 seems to drive an outflow to the south, but its counter flow, if any, has not been detected clearly (Choi 2005). While A1 must be in an evolutionary stage similar to that of A2, the details are less clear.

In this paper, we present the results of our observations of the NGC 1333 IRAS 4A region in the 1.3 cm and 6.9 mm continuum, the NH₃ lines, and the SiO line with an angular resolution higher than those of the previous studies (Choi 2005; Choi et al. 2007). We describe our observations in Section 2. In Section 3, we report the results and discuss the star-forming activities in the IRAS 4A region. A summary is given in Section 4.

2. OBSERVATIONS AND DATA

2.1. K-band Observations

The NGC 1333 IRAS 4 region was observed using the Very Large Array (VLA) of the National Radio Astronomy Observatory in the NH₃ (2, 2) and (3, 3) lines and in the $\lambda = 1.3$ cm continuum. Observations in the C-array configuration were presented in Choi et al. (2007). Details of the observations in the B-array configuration and results for the NH₃ lines were given in Choi et al. (2010). The continuum was observed for 15 minutes at the beginning and for another 15 minutes at the end of each observing track, and the NH₃ lines were observed in the midsection of the track.

For the 1.3 cm continuum, the observations were made in

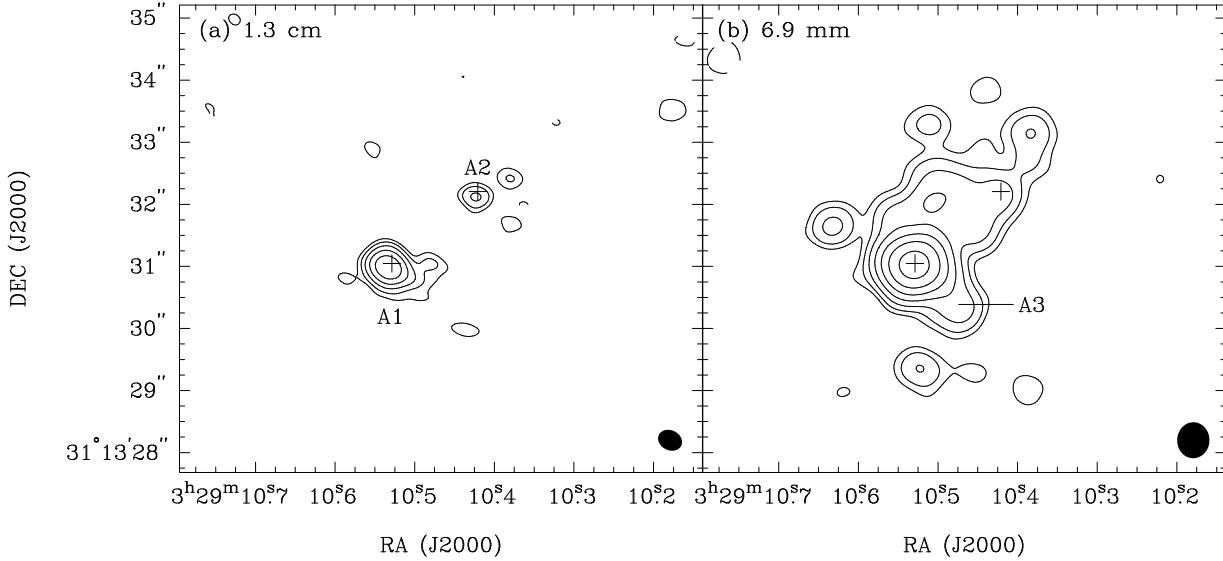


Fig. 1. Maps of the continuum emission toward the NGC 1333 IRAS 4A region. The contour levels are 1, 2, 4, 8, 16, 32, and $64 \times 0.05 \text{ mJy beam}^{-1}$. Dashed contours are for negative levels. (a) Map of the $\lambda = 1.3 \text{ cm}$ continuum made using the B-array data only. The rms noise is $0.016 \text{ mJy beam}^{-1}$. Shown in the bottom right-hand corner is the synthesized beam: $\text{FWHM} = 0''.40 \times 0''.33$ with $\text{PA} = 64^\circ$. (b) Map of the $\lambda = 6.9 \text{ mm}$ continuum. A relatively bright substructure is labeled as A3. The rms noise is $0.017 \text{ mJy beam}^{-1}$. The synthesized beam has $\text{FWHM} = 0''.58 \times 0''.52$ with $\text{PA} = -1^\circ$. Plus signs: the 3.6 cm continuum sources (Reipurth et al. 2002).

the standard K-band continuum mode (22.5 GHz). Maps were made using a CLEAN algorithm. With a natural weighting, the B-array continuum data produced a synthesized beam of $0''.40 \times 0''.33$ in full-width at half-maximum (FWHM).

2.2. Q-band Observations

The NGC 1333 IRAS 4 region was observed using the VLA in the SiO $v = 0 \ J = 1 \rightarrow 0$ line (43.423858 GHz) and in the $\lambda = 6.9 \text{ mm}$ continuum. Twenty-five antennas were used in the C-array configuration on 2004 March 1. The continuum was observed for 20 minutes at the beginning and for 10 minutes at the end of each observing track, and the SiO line was observed in the midsection of the track. For the SiO line, the spectral windows were set to have 64 channels with a channel width of 0.098 MHz, giving a velocity resolution of 0.67 km s^{-1} . For the 6.9 mm continuum, the observations were made in the standard Q-band continuum mode (43.3 GHz).

The phase tracking center was $(\alpha, \delta) = (03^{\text{h}}29^{\text{m}}10^{\text{s}}.993, 31^\circ13'45''.21)$ in J2000.0. Note that the field of view of the C-array observations corresponds to the first field of the D-array mosaic observations (Choi 2005), which covers the northeastern part of the IRAS 4A area including the redshifted outflow of IRAS 4A2. The southwestern field was not covered in the C-array observations, and most part of the blueshifted outflows are outside the field of view.

The nearby quasar 0336+323 (PKS 0333+321) was observed to determine the phase and to obtain the bandpass response. The flux was calibrated by observing the quasar 0713+438 (QSO B0710+439) and by setting its flux density to 0.20 Jy (VLA Calibrator Flux Density Database⁶). To check the flux scale, the quasar 0319+415 (3C 84) was observed in the same track. Comparison of the amplitude gave a flux density of 4.28

Jy for 0319+415, which agrees with the value in the VLA Calibrator Flux Density Database. The bootstrapped flux density of 0336+323 was 1.26 Jy. To avoid the degradation of sensitivity owing to pointing errors, pointing was referenced by observing the calibrators at the X band ($\lambda = 3.6 \text{ cm}$). This referenced pointing was performed about once an hour and just before observing the flux calibrator. With a natural weighting, the SiO data produced a synthesized beam of $\text{FWHM} = 0''.55 \times 0''.52$, and the continuum data produced a beam of $\text{FWHM} = 0''.58 \times 0''.52$.

3. RESULTS AND DISCUSSION

3.1. Continuum Emission Maps

Figure 1 shows the continuum emission maps, and source parameters are listed in Table 1. The 1.3 cm continuum map shows the compact structures of IRAS 4A1 and A2 as well as a few weak features. IRAS 4A1 is marginally resolved, and an elliptical Gaussian fit gives a deconvolved size of $\text{FWHM} = 0''.24 \times 0''.16$ with a position angle (PA) of 52° . IRAS 4A2 is unresolved. The 6.9 mm continuum map shows IRAS 4A1, A2, and an extended structure surrounding the binary system. IRAS 4A2 does not stand out because the extended structure has a comparable brightness. Some of the emission peaks in the extended structure are located away from A1 or A2 with angular distances comparable to the A1-A2 binary separation, which suggests that there is a common envelope around the binary system.

The measurement of total flux is a nontrivial issue, especially for the 6.9 mm map, because the source structure is complicated. The total flux of A1 is not very sensitive to the choice of integration area (a box in this case) because the main peak of A1 is much brighter than the other features in the area. The to-

⁶ See <http://aips2.nrao.edu/vla/calflux.html>.

Table 1. NGC 1333 IRAS 4A Continuum Source Parameters

Source	Peak Position ^a		1.3 cm Flux Density ^b		6.9 mm Flux Density ^b	
	$\alpha_{J2000.0}$	$\delta_{J2000.0}$	Peak	Total	Peak	Total
A1	03 29 10.53	31 13 31.0	1.554 ± 0.016	2.47 ± 0.07	5.57 ± 0.02	9.51 ± 0.12
A2	03 29 10.42	31 13 32.1	0.225 ± 0.016	0.37 ± 0.07	0.39 ± 0.02	1.46 ± 0.08
A	2.66 ± 0.18	...	11.5 ± 0.3

^a Source positions are from the 1.3 cm continuum map. Units of right ascension are hours, minutes, and seconds, and units of declination are degrees, arcminutes, and arcseconds.

^b Flux densities are in mJy beam^{-1} or in mJy, corrected for the primary beam response. The box sizes used for measuring the total flux are the same as those listed in Table 2 of Looney et al. (2000): $2''.9 \times 2''.2$ for A1, $1''.8 \times 1''.6$ for A2, and $5''.4 \times 6''.2$ for A.

tal flux of A2 at 6.9 mm, however, is sensitive to the choice of box because of the extended emission around A2. Since comparisons with the 2.7 mm flux densities are important (see below), we measured the total flux densities (listed in Table 1) in the boxes used by Looney et al. (2000), for consistency in measuring spectral index. However, the A1 and A2 boxes have an overlapping region, and the A box is larger than the union of A1 and A2 boxes. Therefore, the flux density of A is not a simple sum of those of A1 and A2. In the calculation of mass given below, we mostly rely on the 1.3 cm and 2.7 mm total flux densities of the whole IRAS 4A region, and the ambiguity in the 6.9 mm flux density of A2 is not critical.

Figure 2 shows the spectral energy distributions (SEDs) in the centimeter-millimeter wavelength region. SEDs can be described using a power-law form, $F \propto \nu^\alpha$, where F is the flux density, ν is the frequency, and α is the spectral index. Dust emission from a disk/envelope system usually has a large spectral index ($\alpha \gtrsim 2$), and free-free emission from a thermal radio

jet usually has a small spectral index ($\alpha \lesssim 1$) (Reynolds 1986; Anglada et al. 1998). The SED of the IRAS 4A system shows that the slope is steep at shorter wavelengths and shallow at longer wavelengths. The spectral index is large ($\alpha \gtrsim 1.9$) at wavelengths shorter than 3.5 cm, and small ($\alpha \approx 0.6$) in the 6.2–3.5 cm section. This change of α around 3.5 cm suggests that the continuum emission at 1.3 cm and shorter wavelengths mostly comes from dust and that the 6.2 cm continuum may come from free electrons. Even at 3.5 cm, a significant fraction of the flux may come from dust.

The mass of molecular gas can be estimated from the SED of the dust continuum using the mass emissivity given by Beckwith & Sargent (1991),

$$\kappa_\nu = 0.1 \left(\frac{\nu}{\nu_0} \right)^\beta \text{ cm}^2 \text{ g}^{-1}, \quad (1)$$

where $\nu_0 = 1200 \text{ GHz}$, and β is the opacity index. For the 1.3 cm – 2.7 mm section, the opacity index of IRAS 4A is $\beta \approx 1.3$. Assuming optically thin emission, the mass can be estimated by

$$M = \frac{F_\nu D^2}{\kappa_\nu B_\nu(T_d)}, \quad (2)$$

where D is the distance to the source, B_ν is the Planck function, and T_d is the dust temperature.

Assuming $D = 235 \text{ pc}$ and $T_d = 33 \text{ K}$ (Hirota et al. 2008; Jennings et al. 1987), the mass of IRAS 4A is $M = 2.6 \pm 0.8 M_\odot$. The mass estimate is sensitive to the value of β . For example, Looney et al. (2000) derived a mass of $1.3 M_\odot$ (scaled to the distance of 235 pc) assuming $\beta = 1$ and using the 2.7 mm flux density only. Therefore, the uncertainty in mass introduced by the assumptions on β may be about a factor of 2. This mass is based on the flux densities in a box of $5''.4 \times 6''.2$ around IRAS 4A1, which may include the circumstellar disk and protostellar envelope around A1, those around A2, and the common envelope. For comparison, the mass of the whole protostellar envelope of IRAS 4A derived from single-dish observations is $\sim 7 M_\odot$ (Enoch et al. 2009, scaled to 235 pc), and the mass of the IRAS 4A2 protostar derived from the kinematics of the circumstellar disk is $\sim 0.08 M_\odot$ (Choi et al. 2010).

The mass of molecular gas around each protostar can be derived using the ratio of flux densities, assuming that the dust properties are nearly uniform in the whole IRAS 4A system. IRAS 4A1 and A2 are most clearly separated in the 1.3 cm continuum map, and the 1.3 cm flux densities give 2.3 ± 0.7

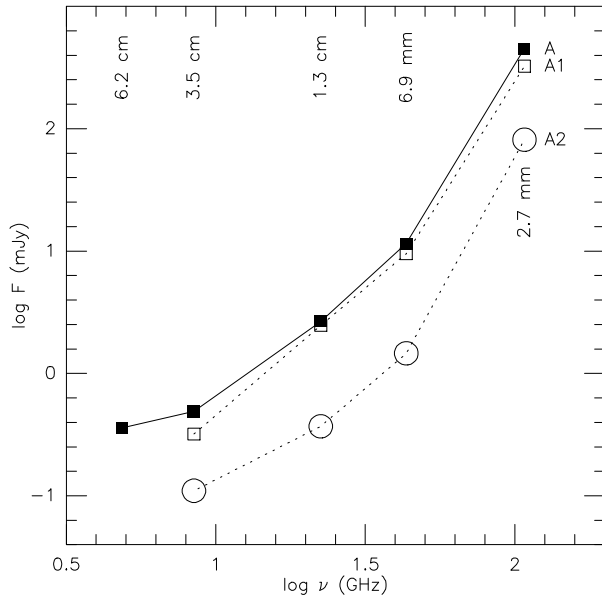


Fig. 2. Spectral energy distributions. Filled squares: IRAS 4A (including A1, A2, and common envelope). Open squares: IRAS 4A1. Open circles: IRAS 4A2. Flux densities are from Rodríguez et al. (1999), Reipurth et al. (2002), this work, and Looney et al. (2000). The flux uncertainties are smaller than the size of markers.

M_{\odot} for A1 and $0.3 \pm 0.1 M_{\odot}$ for A2. Then the total mass of the A2 system (protostar and dense molecular gas) is $\sim 0.4 M_{\odot}$. Therefore, regardless of the mass of the A1 protostar, the A1 system is much more massive than the A2 system.

The extended structure in the 6.9 mm continuum map (Figure 1b) is clumpy and shows several substructures. The overall morphology of the extended structure is similar to what was seen in the 2.7 mm continuum (see Figure 12d of Looney et al. 2000). One of the substructures is relatively bright and can be seen in both the 6.9 mm and 2.7 mm maps. This substructure, labeled as A3 in Figure 1b, has a peak position at $0''.7$ west and $0''.7$ south with respect to A1. The nature of the substructures is not clear. Some of them may be dense clumps in the envelope (that may eventually fall into one of the protostars), some may be prestellar cores, and some might even harbor small compact objects.

3.2. NH_3 Line Maps of the IRAS 4A1 Region

Figure 3 shows high-resolution (B-array) NH_3 maps of the region around IRAS 4A1, and Figure 4 shows the spectra. (See Choi et al. 2007 for NH_3 maps in a lower resolution.) The source structure and spectra of A1 is somewhat different from those of A2 (see Choi et al. 2010 for high-resolution maps of the A2 region). In the case of A2, the NH_3 lines seem to trace the circumstellar disk since the source shape is elongated in the direction perpendicular to the outflow and the spectra has a profile consistent with a rotating disk (Choi et al. 2010). By

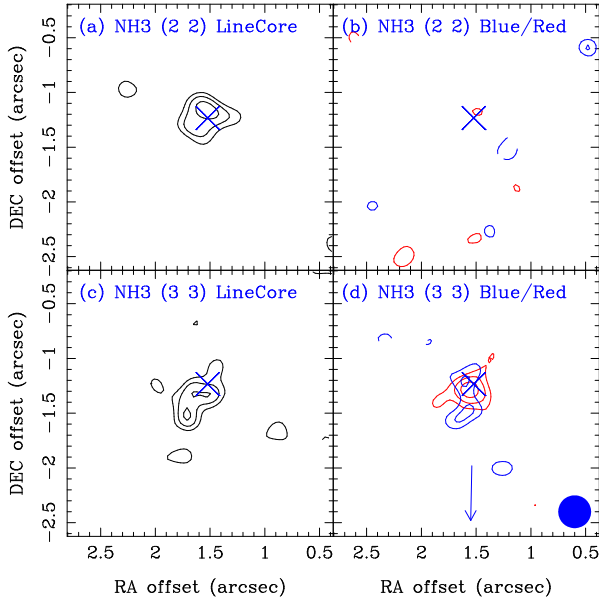


Fig. 3. Maps of the NH_3 lines toward IRAS 4A1 from the VLA B-array data. Contribution from the continuum emission was subtracted out. (a) Map of the (2, 2) line core, $V_{\text{LSR}} = (5.8, 7.6) \text{ km s}^{-1}$. (b) Maps of the blueshifted, $(4.5, 5.8) \text{ km s}^{-1}$, and redshifted, $(7.6, 8.9) \text{ km s}^{-1}$, parts of the (2, 2) line. (c) Map of the (3, 3) line core, $(5.8, 7.6) \text{ km s}^{-1}$. (d) Maps of the blueshifted, $(4.6, 5.8) \text{ km s}^{-1}$, and redshifted, $(7.6, 8.8) \text{ km s}^{-1}$, parts of the (3, 3) line. Contour levels are 3, 4, and 5 times the rms noise [$0.35 \text{ mJy beam}^{-1}$ for (a) and (c), and $0.43 \text{ mJy beam}^{-1}$ for (b) and (d)]. Shown in the bottom right-hand corner is the restoring beam: FWHM = $0''.3$. Cross: peak position of the 1.3 cm continuum. Arrow: direction of the southern outflow (toward outflow peak 16).

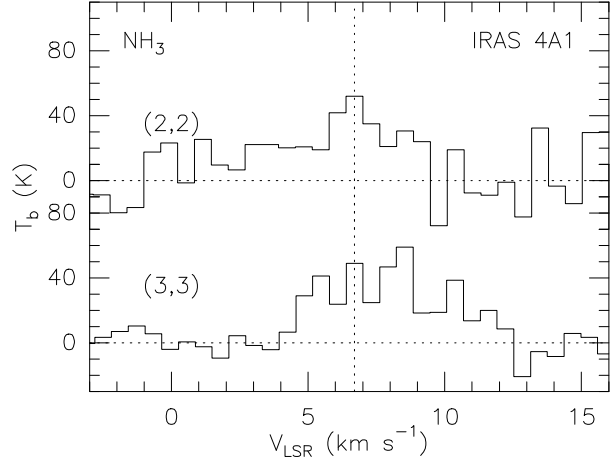


Fig. 4. Spectra of the NH_3 lines toward IRAS 4A1, at the peak position of the 1.3 cm continuum emission. Vertical dotted line: systemic velocity of IRAS 4A ($V_{\text{LSR}} = 6.7 \text{ km s}^{-1}$; Choi 2001).

contrast, the NH_3 maps of A1 show a more complicated morphology, and the spectra of A1 show relatively weak line cores and wider line wings than those of A2. The total integrated NH_3 flux of A1 is smaller than that of A2 by a factor of 1.7.

The (2, 2) line core map (Figure 3a) shows a structure associated with the continuum source. This structure (central component) is elongated in the east-west direction, which may be the circumstellar disk, considering that the blueshifted outflow of A1 is directed toward the south (Choi 2005). The (3, 3) line maps (Figures 3c and 3d) seem to show the central component and a secondary structure about $0''.4$ south (southern component). The southern component is blueshifted and may be related with the southern outflow. The peak positions of the blueshifted and redshifted line wings of the central component (Figure 3d) could not be separated with the $0''.3$ beam, and the rotation of the A1 disk, if any, may be slower than that of the A2 disk. Therefore, the rotation curve could not be analyzed with our data.

In summary, the circumstellar structure of A1 traced by the NH_3 lines seems to be a mixture of the accretion disk and the southern outflow. The A1 disk is weaker than the A2 disk in the NH_3 lines. The rotation of A1 disk seems to be slower than that of A2, suggesting that the A1 protostar is less massive than the A2 protostar.

3.3. Evolutionary Status of the IRAS 4A System

The IRAS 4A system is one of the youngest and best-studied protostar binary systems. The evolutionary status of A2 is especially well-studied thanks to the rotation kinematics of the circumstellar disk (Choi et al. 2010). An interesting issue is the evolutionary status of A1 in comparison with A2.

Previously, Choi et al. (2007) examined the IRAS 4A system with NH_3 and continuum images of $\sim 1''$ resolution. To understand the difference in the NH_3 -to-continuum flux ratios they explored two possibilities: (1) the protostars are exactly coeval, or (2) A2 is a protostar, and A1 may be a transitional object on the verge of protostellar collapse. Because the second possibility contradicts other observational facts, they preferred the

first possibility. However, it implied that the dust-to-gas ratios of A1 and A2 may be quite different, by almost an order of magnitude, which is not easy to understand.

The new higher-resolution images presented in this paper suggest that the difference in the properties of the disks may be the key in understanding the NH_3 -to-continuum flux ratios and also the evolutionary status of the IRAS 4A system. Here we revisit the issue and explore the possibility that A1 and A2 are protostars at slightly different stages of evolution. That is, though A1 and A2 are members of a single binary system, their collapse ages can be different, i.e., not exactly coeval. Then which one is the younger of the two? We suggest that A1 is younger than A2 for several reasons.

First, the accretion disk of A2 traced in the NH_3 lines shows a clearly detectable rotation kinematics, while the A1 disk does not. Since the disk around more massive object rotates faster, the A2 protostar may be more massive than the A1 protostar. Therefore, if the accretion rates are similar, the A1 protostar may be younger than the A2 protostar. (If the accretion rate of A1 is higher, as the envelope of A1 is more massive, then the age of A1 may be even much smaller than that of A2.)

Second, the A2 disk is brighter than the A1 disk in the NH_3 lines. The strength of the NH_3 lines is likely correlated with the mass of the disk, and the disk mass increases monotonically in the simplest models of protostellar evolution (Young & Evans 2005). Therefore, the difference in the NH_3 line strength implies that, if the accretion rates are similar, the A1 disk is less massive and younger than the A2 disk.

Third, the outflow of A2 is much longer than that of A1. The length of the northeast-southwest bipolar outflow driven by A2 is $\sim 130''$ (from the A2 protostar to the H_2 knot HL3; see Figure 1 of Choi et al. 2006). The length of the southern outflow driven by A1 is $\sim 15''$ (from the A1 protostar to the SiO outflow peak 16; see Figure 2a of Choi 2005). Assuming a proper motion of $0''.064 \text{ yr}^{-1}$ (Choi et al. 2006) for rough estimates, the time scale of the A1 outflow is shorter than that of A2 by $\sim 1,800 \text{ yr}$.

The relative youth of A1, despite its relatively massive circumstellar material, suggests that the progenitor prestellar cores evolved at different speeds. As a simplest scenario of the evolution of binary prestellar cores, suppose that the parent cloud fragmented into two cores: core 1 with a mass of M_{C1} that later evolves to become the A1 system, and core 2 with a mass of M_{C2} to become the A2 system. If the collapse age of A2 is indeed larger than that of A1, core 2 may have evolved faster and formed a protostar earlier. Since the denser core evolves faster (that is, the evolution time scale is shorter for the denser core), core 2 may have had a higher density than core 1. This scenario can be understood with a simple argument. At the time of the fragmentation, suppose that each of the two cores has a roughly spherical shape (or any shape similar to each other), and the boundary (the point of contact between the two spheres) is the point where the gravitational forces of the two cores balance out. Then the ratio of radii is $R_{C1}/R_{C2} \approx \sqrt{M_{C1}/M_{C2}}$, and the density ratio is $n_{C1}/n_{C2} \approx 1/\sqrt{M_{C1}/M_{C2}}$. Though the exact density ratio may depend on details of the fragmentation process, the more massive core may usually have a smaller average density

than the sibling core. (For the IRAS 4A system, if the mass ratio at the time of fragmentation is similar to the current value, $M_{C1}/M_{C2} \approx M_{A1}/M_{A2} \approx 6$ and $n_{C1}/n_{C2} \approx 0.4$.) Therefore, it is reasonable that, when a cloud fragments into two cores, the less massive one would be denser, evolve faster, and form a protostar earlier. Considering the amount of circumstellar material, however, A1 may outgrow A2 in the future and eventually become a more massive star.

If A1 is indeed younger than A2, how large is the age gap? To answer this question, the collapse age of A1 needs to be measured using the rotation kinematics of the disk, as what was done with A2, which requires imaging with a resolution higher than ours. Instead, here we simply calculate a characteristic time scale of the system as a sketchy expectation based on simple physics. The age gap may be in the order of a time scale that governs the dynamics of the A1-A2 system, i.e., a sound-crossing time. Assuming an effective sound speed of 0.27 km s^{-1} (Young & Evans 2005), the projected separation of $1''.8$ (430 AU) gives a sound-crossing time of $\sim 7,500 \text{ yr}$. Considering that the A1-A2 system is not necessarily in the plane of the sky, the value above is a lower limit. For example, if we assume that the A1-A2 system is $\sim 30^\circ$ out of the plane of the sky, the sound-crossing time would be $\sim 9,000 \text{ yr}$, which is $\sim 20\%$ of the collapse age of A2. (See Figure 5 for the comparison between the binary separation and the infall region.)

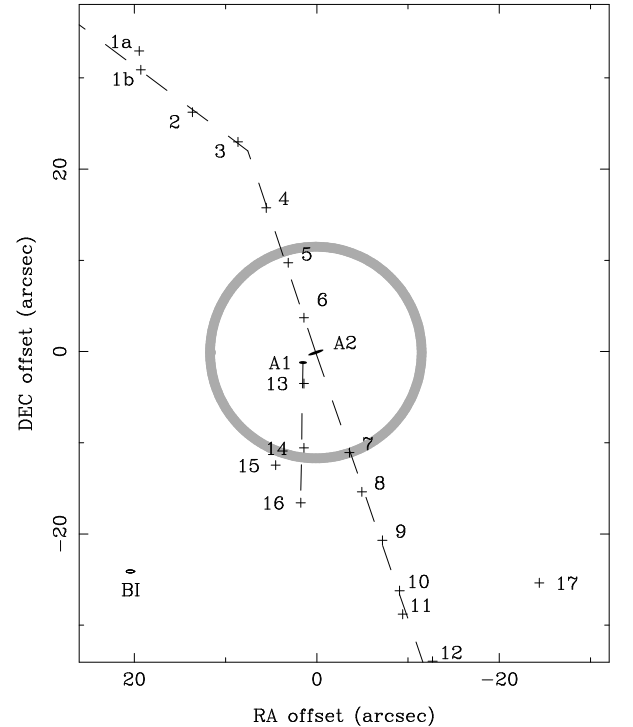
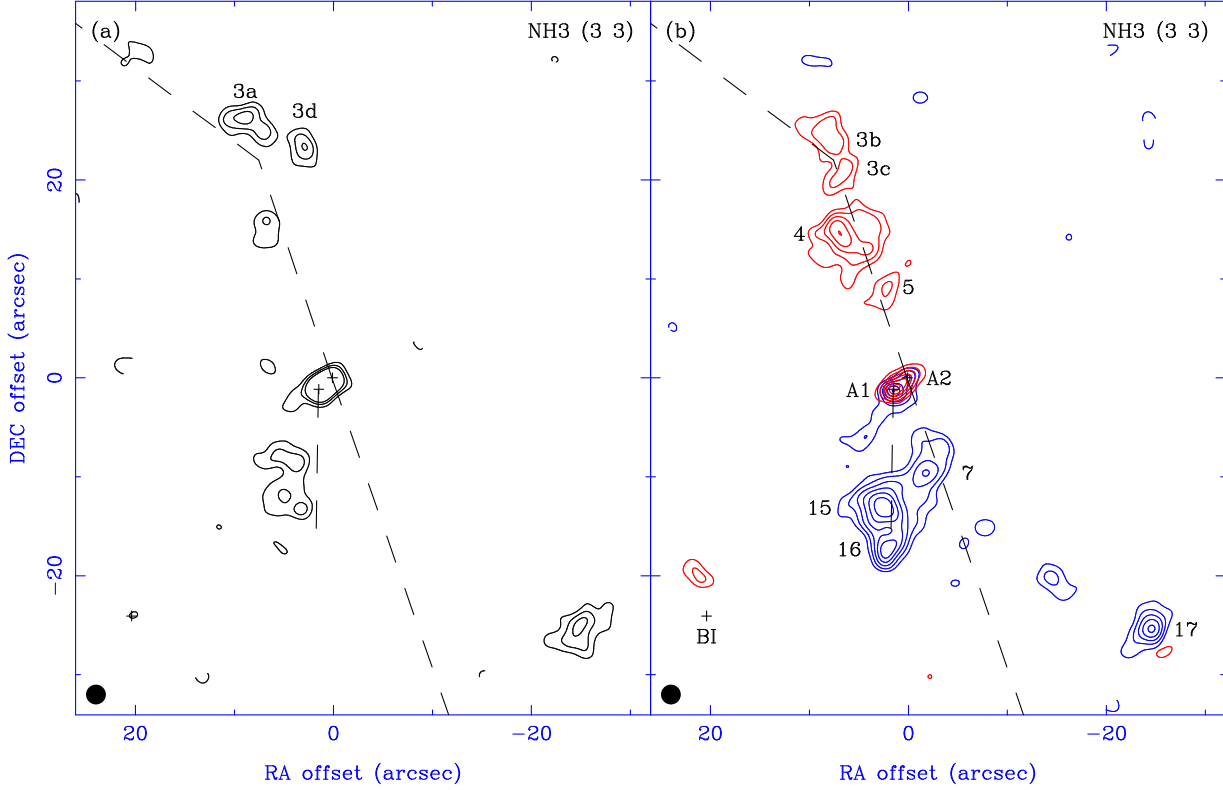


Fig. 5. Schematic diagram of the IRAS 4A system. Protostars A1, A2, and BI are labeled. Plus signs: SiO outflow peaks. See Figure 2a of Choi (2005). Dashed lines: outflow axes. Gray circle: infall region with a radius of 2,700 AU, which corresponds to the size of the spherical collapse wave with a sound speed of 0.27 km s^{-1} and a collapse age of 50,000 yr.



[See <http://minho.kasi.re.kr/Publications.html> for the original figure.]

Fig. 6. Maps of the NH_3 (3, 3) line toward the IRAS 4A region, made from the VLA C-array data (also see Figure 1 of Choi et al. 2007). The maps were convolved to have an angular resolution of $\text{FWHM} = 2''.0$ as shown in the bottom left-hand corner. For these maps, the continuum levels were not subtracted from the line data, and the structure associated with IRAS 4A1, A2, and BI comes from both the continuum and line emission. (a) Map of the line core. Black contours show the intensity distribution averaged over the velocity interval of $V_{\text{LSR}} = (5.8, 7.6) \text{ km s}^{-1}$. Contour levels are 3, 4, and 5 times the rms noise ($0.7 \text{ mJy beam}^{-1}$). (b) Maps of the line wings. Blue and red contours are for the velocity intervals of $(-1.0, 5.8)$ and $(7.6, 14.4) \text{ km s}^{-1}$, respectively. Contour levels are 3, 4, 5, 6, 7, and 8 times the rms noise ($0.4 \text{ mJy beam}^{-1}$). Some outflow peaks are labeled (also see Figure 5). Gray scale: map of the $\text{SiO } v = 0 \text{ } J = 1 \rightarrow 0$ line (Figure 3a of Choi 2005). Plus signs: the 3.6 cm continuum sources (Reipurth et al. 2002).

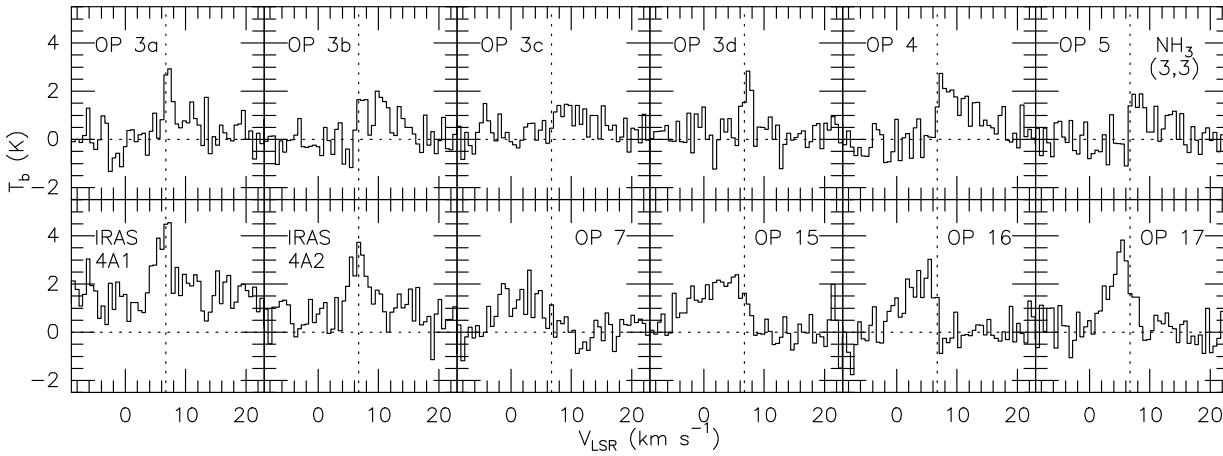


Fig. 7. Spectra of the NH_3 (3, 3) line from the C-array maps with an angular resolution of $2''.0$ (Figure 6) toward several NH_3 outflow peaks and IRAS 4A1/2. Vertical dotted line: systemic velocity of IRAS 4A.

3.4. Outflows

The molecular outflows in the IRAS 4A region were detected in the NH_3 (3, 3) line but almost undetected in the (2, 2) line. Since some weak emission structures of the outflows tend to be buried by noise when the nominal synthesized beams were

used, the maps were convolved with larger beams to show the outflows clearly. Figure 5 shows a schematic diagram of the IRAS 4A system, and Figure 6 shows NH_3 (3, 3) line maps with an angular resolution of $2''$. Figure 7 shows the spectra at outflow peak positions. Figure 8 shows the NH_3 (3, 3) line map

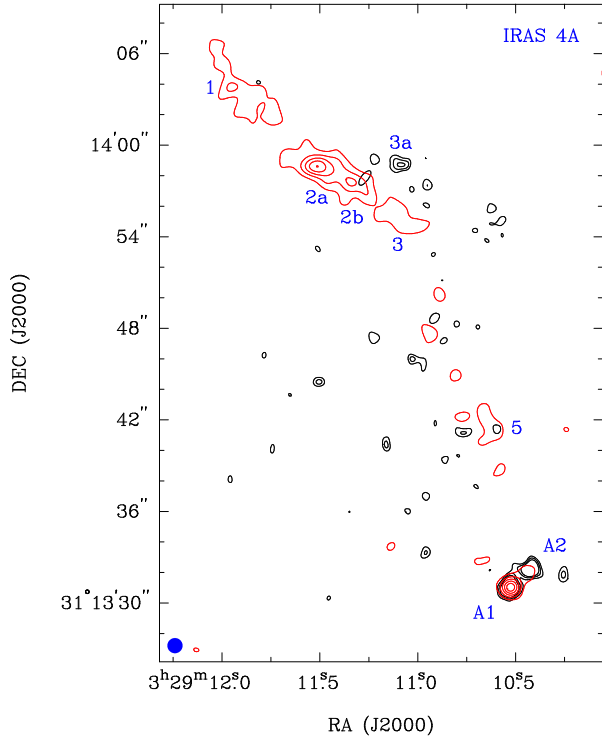


Fig. 8. Maps of the northeastern area of the IRAS 4A region. The continuum levels were not subtracted from the line data. Black contours: map of the NH_3 (3, 3) line from the VLA C-array data, averaged over the velocity interval of $V_{\text{LSR}} = (6.4, 7.6) \text{ km s}^{-1}$. Contour levels are 3, 4, and 5 times the rms noise ($0.5 \text{ mJy beam}^{-1}$). Negative levels are not shown, to avoid clutter. Shown in the bottom left-hand corner is the synthesized beam: $\text{FWHM} = 0''.98 \times 0''.95$ with $\text{PA} = 47^\circ$. Red contours: map of the $\text{SiO } v=0 J=1 \rightarrow 0$ line from the VLA C-array data, averaged over the velocity interval of $(7.7, 25.9) \text{ km s}^{-1}$. Contour levels are 1, 2, 3, 4, and $5 \times 0.5 \text{ mJy beam}^{-1}$, and the rms noise is $0.18 \text{ mJy beam}^{-1}$. The SiO map was convolved to have an angular resolution of $\text{FWHM} = 1''.0$. Protostars and outflow peaks are labeled.

with an angular resolution of $1''$ for the velocity range showing the outflow peak (OP) 3a clearly. Figure 8 also shows the SiO line map showing the northeastern jet of IRAS 4A2. For these maps (Figures 6 and 8), contributions from the continuum emission were not removed because the velocity extents of the line wings at strong peaks are comparable to the spectral coverage and left only a little room for line-free channels that can be used for determining the continuum levels. The structures directly associated with the continuum sources in these maps should be ignored.

In general, most of the NH_3 peaks associated with the IRAS 4A1/2 outflows are located on or near the SiO outflow peaks (Figure 6b), but the intensity distributions are quite different. In the SiO outflow maps, the strongest redshifted emission comes from OP 1 and 2, and the strongest blueshifted emission comes from OP 7 and 9. By contrast, in the NH_3 maps, OP 3 and 4 are the strongest redshifted peaks, and OP 15 and 16 are the strongest blueshifted peaks.

OP 17 is unusually strong in the NH_3 line, but the nature of this source is not clear (Lefloch et al. 1998; Choi 2005). In addition to the IRAS 4A outflows, the NH_3 map also shows the outflow associated with IRAS 4BI (the redshifted emission at

$\sim 4''$ north of BI in Figure 6b).

3.5. Deflection of the Northeastern Outflow

One of the most interesting properties of the IRAS 4A2 outflow is the directional variability of the northeastern (redshifted) jet. The change of flow direction, or a sharp bend, near OP 3 is a good example of jet deflection caused by a collision with a dense core in the ambient cloud (Choi 2005). Figure 8 shows the detailed structure of the SiO jet, and Figure 9 shows the spectra. The undeflected upstream part (OP 3–5) is weak in the SiO line. The deflected downstream part (OP 1–3) is relatively strong in the SiO line. OP 2 in the low-resolution map (Choi 2005) is now resolved into two peaks (OP 2a and 2b) in the new map. Though these two peaks are spatially close to each other (within $2''.5$ or 600 AU), their velocity structures are very different: OP 2a has double peaks (one at 17 and the other at 21 km s^{-1}), and OP 2b has a single peak (at 18 km s^{-1}). This sudden change of velocity structure suggests that the deflected jet is highly turbulent.

One of the motivations of the new high-resolution observations was imaging the detailed structure of the jet at the jet-core impact point that is supposed to be near OP 3. However, the SiO emission of OP 3 is weak and does not show a compact structure, which may mean that the SiO emission does not get bright immediately after the impact but takes some time to develop. A likely explanation is that Si atoms in dust grains are injected into the shocked gas at the impact point, combine with oxygen in the gas, and form SiO in a time scale of 100–1,000 yr (Schilke et al. 1997; Gusdorf et al. 2008; Guillet et al. 2009). The SiO molecules then combine again with oxygen and be-

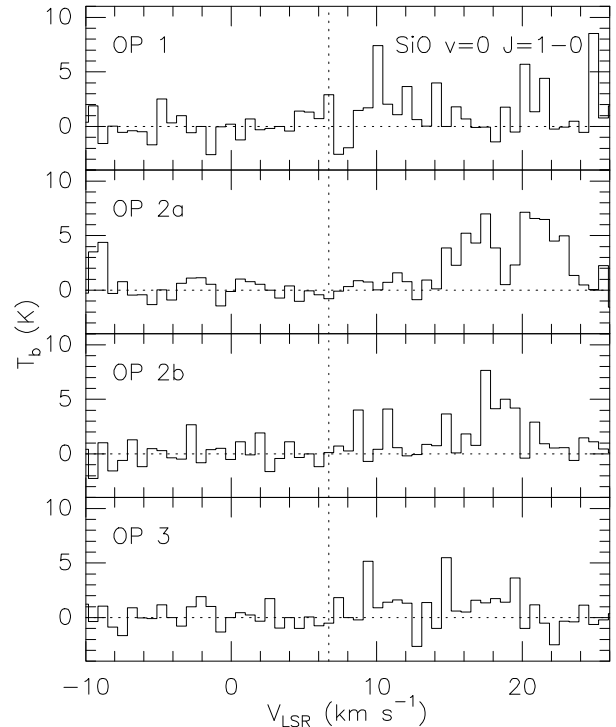
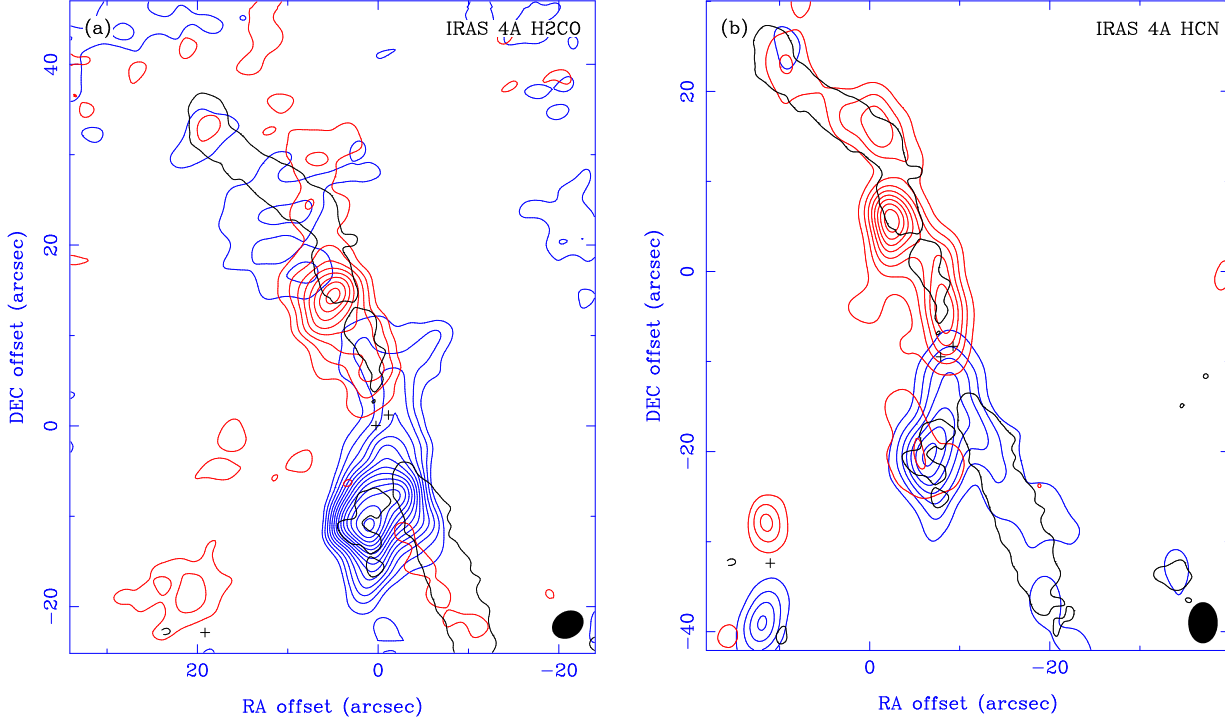


Fig. 9. Spectra of the SiO line toward SiO outflow peaks 1–3 (see Figure 8 for the positions of the outflow peaks). Vertical dotted line: systemic velocity of IRAS 4A.



[See <http://minho.kasi.re.kr/Publications.html> for the original figure.]

Fig. 10. Maps of the molecular outflows in the IRAS 4A region. For these maps, continuum levels were subtracted out. (a) Maps of the H₂CO 141 GHz line (Choi et al. 2004). Blue and red contours show the intensity distribution averaged over the velocity intervals of $V_{\text{LSR}} = (-1.0, 5.8)$ and $(7.7, 14.4)$ km s⁻¹, respectively. The lowest contour level and the contour interval are 70 mJy beam⁻¹, and the rms noise is 22 mJy beam⁻¹. Negative levels are not shown, to avoid clutter. (b) Maps of the HCN $J = 1 \rightarrow 0$ line (Choi 2001). See Figures 1 and 2 of Choi (2001) for the velocity intervals. Note that the blueshifted and redshifted line wings cannot be clearly separated because of the blending of hyperfine components. The lowest contour level and the contour interval are 60 mJy beam⁻¹, and the rms noise is 20 mJy beam⁻¹. Gray scale: map of the SiO line (Figure 3a of Choi 2005). Plus signs: the 3.6 cm continuum sources (Reipurth et al. 2002).

come SiO₂. Therefore, the strength of the SiO emission would peak with a certain time lag after the jet-core impact.

In the deflected jet of IRAS 4A2, the SiO emission is brightest at OP 2a, $\sim 7''$ from the sharp bend. There is no measurement of the proper motion in this part of the outflow. If we use the proper motion measured in the southwestern jet ($0.''064$ yr⁻¹; Choi et al. 2006) as a very rough guide, the time scale of outflow propagation from the impact point to OP 2a is ~ 100 yr. The argument above assumes that the jet is a steady flow, but images of the IRAS 4A2 jet show that the brightness distribution is far from uniform. The brightness distribution of the deflected jet would also be subject to the non-steady structure of the impacting jet. Considering the average separation between outflow peaks, the uncertainty in the time scale of SiO peak emission would be $\sim 40\%$.

The NH₃ maps (Figures 6 and 8) show an interesting structure around OP 3. While the emission peaks directly associated with the outflow (OP 3b and 3c) show wide redshifted line wings, those located slightly away from the SiO jet (OP 3a and 3d) show narrow lines near the ambient velocity (Figure 7). OP 3a and 3d are probably parts of the dense core that is obstructing the northeastern jet and causing the deflection. NH₃ molecules at OP 3a is excited either by the shock propagated from the impact point or by a stream of jet that penetrated deep into the obstructing core. Examinations of the centimeter-millimeter continuum maps show that there is no detectable continuum source at or near the position of OP 3a (Rodríguez

et al. 1999; Reipurth et al. 2002; Choi et al. 2004, 2007; this work).

3.6. Outflow Chemistry

As mentioned above, there is an interesting difference between the intensity distributions of SiO and NH₃. Comparisons with other outflow tracers would be helpful in understanding the intensity distributions. Figure 10 shows the H₂CO and HCN maps of the IRAS 4A outflows (Choi 2001; Choi et al. 2004). The outflow structure in SiO is most well-collimated and straight, and the outflow images in the other tracers agree with the SiO image in the overall structure. Outflow peaks in the four tracers are usually located close to each other. Especially, OP 1, 3, 4, and 15 are detectable in all the four outflow maps, and the peak positions of each OP in these maps are clustered within $\sim 2''$. (The average separation between adjacent peaks is $\sim 6''$.) This clustering suggests that a single physical agent (e.g., internal shock in the primary jet) is responsible for the excitation of all the four outflow tracers. Therefore, the outflowing gas components traced by these tracers are physically closely connected to each other and flow with a certain degree of coherence.

Though the outflow tracers share the source of excitation, SiO stands out when the intensity distributions are compared. In the northern part of the IRAS 4A region, the SiO map shows that the deflected (downstream) part of the northeastern jet (OP 1–3) is brighter than the undeflected (upstream) part (OP 3–5).

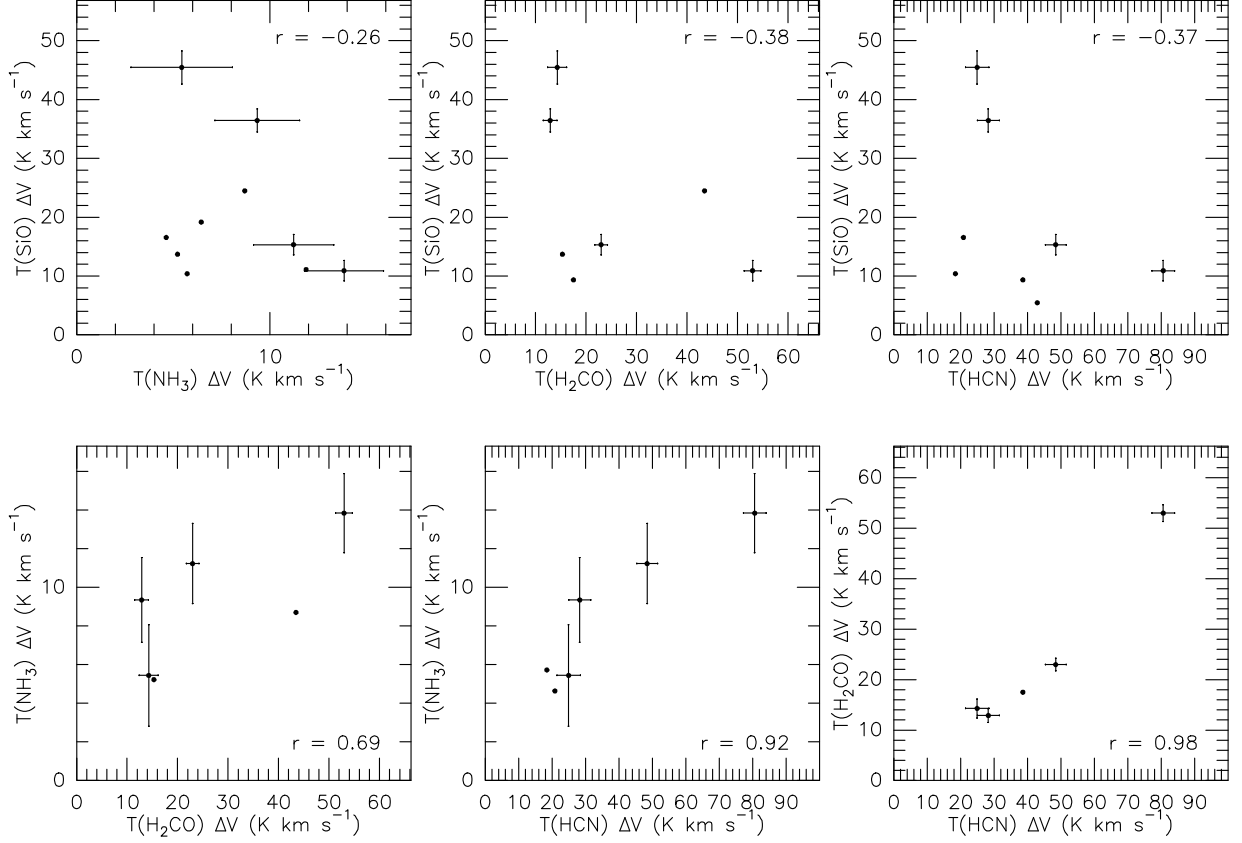


Fig. 11. Correlation diagrams of the SiO, NH₃, H₂CO, and HCN line intensities for outflow peaks (see the maps in Figures 6b, 10a, and 10b). The integrated intensities are corrected for the primary beam response. Uncertainties are marked for outflow peaks 1, 3, 4, and 15. Written in the top/bottom right-hand corners are the linear correlation coefficients.

The maps of the other tracers show that the upstream part is brighter. In the southern part of the region, the SiO map shows that the southwestern jet (blueshifted jet of IRAS 4A2: OP 7–12) is brighter than the southern outflow (blueshifted outflow of IRAS 4A1: OP 13–16). The maps of the other tracers show that the southern outflow (especially OP 15 and 16) is brighter. The intensity distribution pattern of the NH₃, H₂CO, and HCN maps is similar to that of the CO $J = 2 \rightarrow 1$ outflow map (see Figure 1 of Girart et al. 1999).

To show this trend quantitatively, correlation diagrams of the outflow peaks were made. The intensity of the SiO line tends to be anti-correlated with those of the other lines (Figure 11, top panels). The linear correlation coefficients are negative: $r \approx -0.3$. If only the outflow peaks detected in all the four lines are considered (marked with uncertainty bars in Figure 11), the anti-correlation is even stronger: $r \approx -0.9$. By contrast, the intensities are positively correlated among NH₃, H₂CO, and HCN: $r \approx 0.9$ (Figure 11, bottom panels). This difference suggests that the outflow component traced by SiO is fundamentally different from that of the other tracers.

Blake et al. (1995) arrived at a similar conclusion based on the spectral profiles of molecular lines obtained from single-dish observations, which show that the SiO emission is kinematically displaced from the bulk cloud velocity. The image and spectra of the SiO line suggests that the gas traced by the SiO emission is either the primary jet itself or an outflow com-

ponent closely linked to the primary jet, as suggested by the observations of other outflows such as L1448 and HH 212 (Dutrey et al. 1997; Codella et al. 2007).

The dichotomy between SiO and the other outflow tracers can be explained in two different ways. First, the differences in shock strength may trigger different chemical processes. While the sputtering of Si from dust grains requires shock velocities higher than $\sim 25 \text{ km s}^{-1}$, species such as H₂CO do not survive at such high velocities (Blake et al. 1995; Schilke et al. 1997; Arce et al. 2007). In this scenario, the intensity ratio of SiO to the other species can be an indicator of the shock strength. Second, the line intensities may be tracing either different physical properties or different regions of the outflow system. While SiO may reflect the shock strength of the jet itself, the other tracers may reflect physical conditions of the ambient medium such as the density of ambient cloud (Blake et al. 1995).

4. SUMMARY

The NGC 1333 IRAS 4A region was observed using the VLA in the 1.3 cm and 6.9 mm continuum, the NH₃ (2, 2) and (3, 3) lines, and the SiO $v = 0 \ J = 1 \rightarrow 0$ line, with an angular resolution of $\sim 0''.4$, to image the circumstellar structures and outflows of the protobinary system. The continuum emission mostly comes from dust in the circumstellar disks

and the protostellar envelopes. The high-resolution ($0''.3$) images of the NH_3 lines show the detailed structures of the disks and outflows around the protostars. The molecular line images of relatively low resolutions ($1''$ – $2''$) were used to investigate the properties of the protostellar outflows. The main results are summarized as follows.

1. The continuum maps show two compact emission sources and a clumpy extended structure surrounding them. They may include the circumstellar disks, protostellar envelopes, and the common envelope of the binary system. The steep SED suggests that most of the 1.3 cm and 6.9 mm continuum emission comes from dust. The mass of the dense molecular gas in the binary system, imaged by the millimeter-continuum interferometric observations, is $\sim 2.6 M_\odot$. The IRAS 4A1 protostar-disk-envelope system is more massive than the A2 system by a factor of ~ 6 .

2. The NH_3 line maps of the region immediately around IRAS 4A1 show at least two components. One is probably the circumstellar disk, and the other may be the blueshifted southern outflow. The blueshifted and redshifted emission sources of the central (disk) component was not spatially separated, suggesting that the disk may be rotating relatively slowly. Analysis of the rotation curve, as what was done with the A2 disk, was not possible with the angular resolution of this work, and suggests that the A1 protostar is less massive than the A2 protostar.

3. Considering the properties of the disks and the lengths of the outflows, IRAS 4A1 may be younger than A2, in terms of collapse age. We suggest that the less massive member of a binary prestellar core system may start the protostellar collapse earlier than its companion.

4. The molecular outflows are brighter in the NH_3 (3, 3) line than in the (2, 2) line. The overall structure of the NH_3 outflows is similar to that of the SiO jets/outflows, though there are interesting differences in small-scale structures and intensity distributions.

5. The $1''$ resolution map of the SiO line shows the highly turbulent structures of the deflected part of the IRAS 4A2 northeastern jet. The SiO line is brightest at a peak located $\sim 7''$ from the starting point of the deflected part, suggesting that the enhancement of SiO in the jet takes ~ 100 yr after the proposed jet-core collision. The NH_3 line maps show an ambient-velocity structure near the impact point, which may be a part of the obstructing dense cloud core.

6. Comparisons of the SiO, NH_3 , H_2CO , and HCN maps of the IRAS 4A outflows show an interesting chemical dichotomy. The intensity distribution of SiO is anti-correlated with those of the others. This trend suggests that NH_3 , H_2CO , and HCN may trace the same bulk of gas in the molecular outflows, while SiO traces a gas component more directly related to the primary jet.

We thank Jongsoo Kim for helpful discussions. M. C. and M. K. were supported by the Core Research Program of the National Research Foundation of Korea (NRF) funded by the Ministry of Education, Science and Technology (MEST) of

the Korean government (grant number 2011-0015816). J.-E. L. was supported by the Basic Science Research Program through NRF funded by MEST (grant number 2011-0004781). The National Radio Astronomy Observatory is a facility of the National Science Foundation operated under cooperative agreement by Associated Universities, Inc.

References

- Anglada, G., Villuendas, E., Estalella, R., Beltrán, M. T., Rodríguez, L. F., Torrelles, J. M., & Curiel, S. 1998, *AJ*, 116, 2953
- Arce, H. G., Shepherd, D., Gueth, F., Lee, C.-F., Bachiller, R., Rosen, A., & Beuther, H. 2007, in *Protostars and Planets V*, ed. B. Reipurth, D. Jewitt, & K. Keil (Tucson, AZ: Univ. Arizona Press), 245
- Baek, C. H., Kim, J., & Choi, M. 2009, *ApJ*, 690, 944
- Beckwith, S. V. W., & Sargent, A. I. 1991, *ApJ*, 381, 250
- Blake, G. A., Sandell, G., van Dishoeck, E. F., Groesbeck, T. D., Mundy, L. G., & Aspin, C. 1995, *ApJ*, 441, 689
- Choi, M. 2001, *ApJ*, 553, 219
- Choi, M. 2005, *ApJ*, 630, 976
- Choi, M., Hodapp, K. W., Hayashi, M., Motohara, K., Pak, S., & Pyo, T.-S. 2006, *ApJ*, 646, 1050
- Choi, M., Kamazaki, T., Tatematsu, K., & Panis, J.-F. 2004, *ApJ*, 617, 1157
- Choi, M., Kang, M., & Tatematsu, K. 2011, *ApJ*, 728, L34
- Choi, M., Tatematsu, K., & Kang, M. 2010, *ApJ*, 723, L34
- Choi, M., Tatematsu, K., Park, G., & Kang, M. 2007, *ApJ*, 667, L183
- Codella, C., Cabrit, S., Gueth, F., Cesaroni, R., Bacciotti, F., Lefloch, B., & McCaughrean, M. J. 2007, *A&A*, 462, L53
- Dutrey, A., Guilloteau, S., & Bachiller, R. 1997, *A&A*, 325, 758
- Enoch, M. L., Evans, N. J., II, Sargent, A. I., & Glenn, J. 2009, *ApJ*, 692, 973
- Girart, J. M., Crutcher, R. M., & Rao, R. 1999, *ApJ*, 525, L109
- Guillet, V., Jones, A. P., & Pineau des Forêts, G. 2009, *A&A*, 497, 145
- Gusdorf, A., Cabrit, S., Flower, D. R., & Pineau des Forêts, G. 2008, *A&A*, 482, 809
- Hirota, T., et al. 2008, *PASJ*, 60, 37
- Hodapp, K.-W., & Ladd, E. F. 1995, *ApJ*, 453, 715
- Jennings, R. E., Cameron, D. H. M., Cudlip, W., & Hirst, C. J. 1987, *MNRAS*, 226, 461
- Jørgensen, J. K., et al. 2007, *ApJ*, 659, 479
- Lay, O. P., Carlstrom, J. E., & Hills, R. E. 1995, *ApJ*, 452, L73
- Lefloch, B., Castets, A., Cernicharo, J., & Loinard, L. 1998, *ApJ*, 504, L109
- Looney, L. W., Mundy, L. G., & Welch, W. J. 2000, *ApJ*, 529, 477
- Marvel, K. B., Wilking, B. A., Claussen, M. J., & Wootten, A. 2008, *ApJ*, 685, 285
- Park, G., & Choi, M. 2007, *ApJ*, 664, L99
- Reipurth, B., Rodríguez, L. F., Anglada, G., & Bally, J. 2002, *AJ*, 124, 1045
- Reynolds, S. P. 1986, *ApJ*, 304, 713
- Rodríguez, L. F., Anglada, G., & Curiel, S. 1999, *ApJS*, 125, 427
- Sandell, G., Aspin, C., Duncan, W. D., Russell, A. P. G., & Robson, E. I. 1991, *ApJ*, 376, L17
- Schilke, P., Walmsley, C. M., Pineau des Forêts, G., & Flower, D. R. 1997, *A&A*, 321, 293
- Young, C. H., & Evans, N. J., II 2005, *ApJ*, 627, 293